Physics and Imaging in Radiation Oncology 17 (2021) 13–19

Contents lists available at ScienceDirect

Physics and Imaging in Radiation Oncology

journal homepage: www.sciencedirect.com/journal/physics-and-imaging-in-radiation-oncology

Evaluation of the radiofrequency performance of a wide-bore 1.5 T positron emission tomography/magnetic resonance imaging body coil for radiotherapy planning

Woutjan Branderhorst [a,*], Bart R. Steensma [a], Casper Beijst [a], Erik R. Huijing [a], Cezar Alborahal [a], Edwin Versteeg [a], Bjoern Weissler [b], David Schug [b], Pierre Gebhardt [b], Nicolas Gross-Weege [b], Florian Mueller [b], Karl Krueger [b], Thomas Dey [b], Harald Radermacher [b], Oliver Lips [c], Jan Lagendijk [a], Volkmar Schulz [b], Hugo W.A.M. de Jong [a], Dennis W.J. Klomp [a]

[a] Department of Radiology and Nuclear Medicine, University Medical Center Utrecht, Utrecht, The Netherlands
[b] Department of Physics of Molecular Imaging Systems, RWTH Aachen University, Aachen, Germany
[c] Philips Research Europe, Hamburg, Germany

ARTICLE INFO

Keywords:
PET/MRI
Radiotherapy
Body coil
Wide bore
RF shielding
Treatment planning

ABSTRACT

Background and purpose: The restricted bore diameter of current simultaneous positron emission tomography/magnetic resonance imaging (PET/MRI) systems can be an impediment to achieving similar patient positioning during PET/MRI planning and radiotherapy. Our goal was to evaluate the B_1 transmit (B_1^+) uniformity, B_1^+ efficiency, and specific absorption rate (SAR) of a novel radiofrequency (RF) body coil design, in which RF shielded PET detectors were integrated with the specific aim of enabling a wide-bore PET/MRI system.

Materials and methods: We designed and constructed a wide-bore PET/MRI RF body coil to be integrated with a clinical MRI system. To increase its inner bore diameter, the PET detectors were positioned between the conductors and the RF shield of the RF body coil. Simulations and experiments with phantoms and human volunteers were performed to compare the B_1^+ uniformity, B_1^+ efficiency, and SAR between our design and the clinical body coil.

Results: In the simulations, our design achieved nearly the same B_1^+ field uniformity as the clinical body coil and an almost identical SAR distribution. The uniformity findings were confirmed by the physical experiments. The B_1^+ efficiency was 38% lower compared to the clinical body coil.

Conclusions: To achieve wide-bore PET/MRI, it is possible to integrate shielding for PET detectors between the body coil conductors and the RF shield without compromising MRI performance. Reduced B_1^+ efficiency may be compensated by adding a second RF amplifier. This finding may facilitate the application of simultaneous whole-body PET/MRI in radiotherapy planning.

1. Introduction

The development of clinical whole-body positron emission tomography/magnetic resonance imaging (PET/MRI) systems has stimulated research on possibilities to apply PET/MRI for treatment planning and diagnostic workup of image-guided radiotherapy [1–5]. Previous simultaneous PET/MRI designs were typically based on the concept of adding PET scintillation crystals and readout electronics to an existing MRI system [6], either in the form of a removable PET insert (e.g. for small-animal [7–9] or brain [10–12]), or integrated between the gradient coil and the RF body coil (e.g. [13,14]). Whereas the removable insert designs typically required a relatively small inner bore size that allowed an easy fit into a whole-body MRI system, the designers of integrated clinical whole-body systems had to optimize the trade-off between increasing scanner performance and maximizing the space inside the PET ring. Consequently, there are currently no simultaneous PET/MRI systems having an inner bore diameter larger than 60 cm [13–15]. The confined bore size has been an important limitation of current clinical PET/MRI systems when applied for treatment planning and diagnostic workup of image-guided therapies, which often required a larger bore to

* Corresponding author at: Department of Radiology and Nuclear Medicine, University Medical Center Utrecht, P.O. Box 85500, 3508 GA Utrecht, The Netherlands.

https://doi.org/10.1016/j.phro.2020.12.002
Received 15 June 2020; Received in revised form 17 November 2020; Accepted 9 December 2020
Available online 23 December 2020

scan the patient in the same position as during therapy (e.g. with the arms upwards, or using large immobilization and positioning aids).

To address this limitation, we investigated the possibility of increasing the inner bore diameter by integrating the PET detectors into the confined space between the RF shield and the conductors of the RF body coil. To prevent mutual interference with the MRI system, PET detectors must be shielded [16]. Placing metal shields close to the conductors of the body coil results in eddy currents and a reduction in B_1^+ efficiency and uniformity during MRI. We have built a prototype PET/MRI body coil with a special design of the PET detector shieldings aimed at reducing these adverse effects.

The purpose of this study was to evaluate the B_1^+ uniformity, B_1^+ efficiency, and specific absorption rate (SAR) of our new body coil design with RF shields for integrated PET detectors. The novelty in our body coil design was that the PET detectors and shielding are positioned in the gap between the gradient RF shield and the RF body coil. Compared to other designs, in which this gap contains no conductive materials for efficiency reasons, this strategy reduced the amount of bore diameter that needed to be compromised to accommodate PET components.

2. Materials and methods

2.1. Design of the wide-bore PET/MRI body coil

Our high-pass quadrature birdcage (~64 MHz) body coil design, shown in Fig. 1A, had 38 RF rungs of length 45 cm. While 38 could not

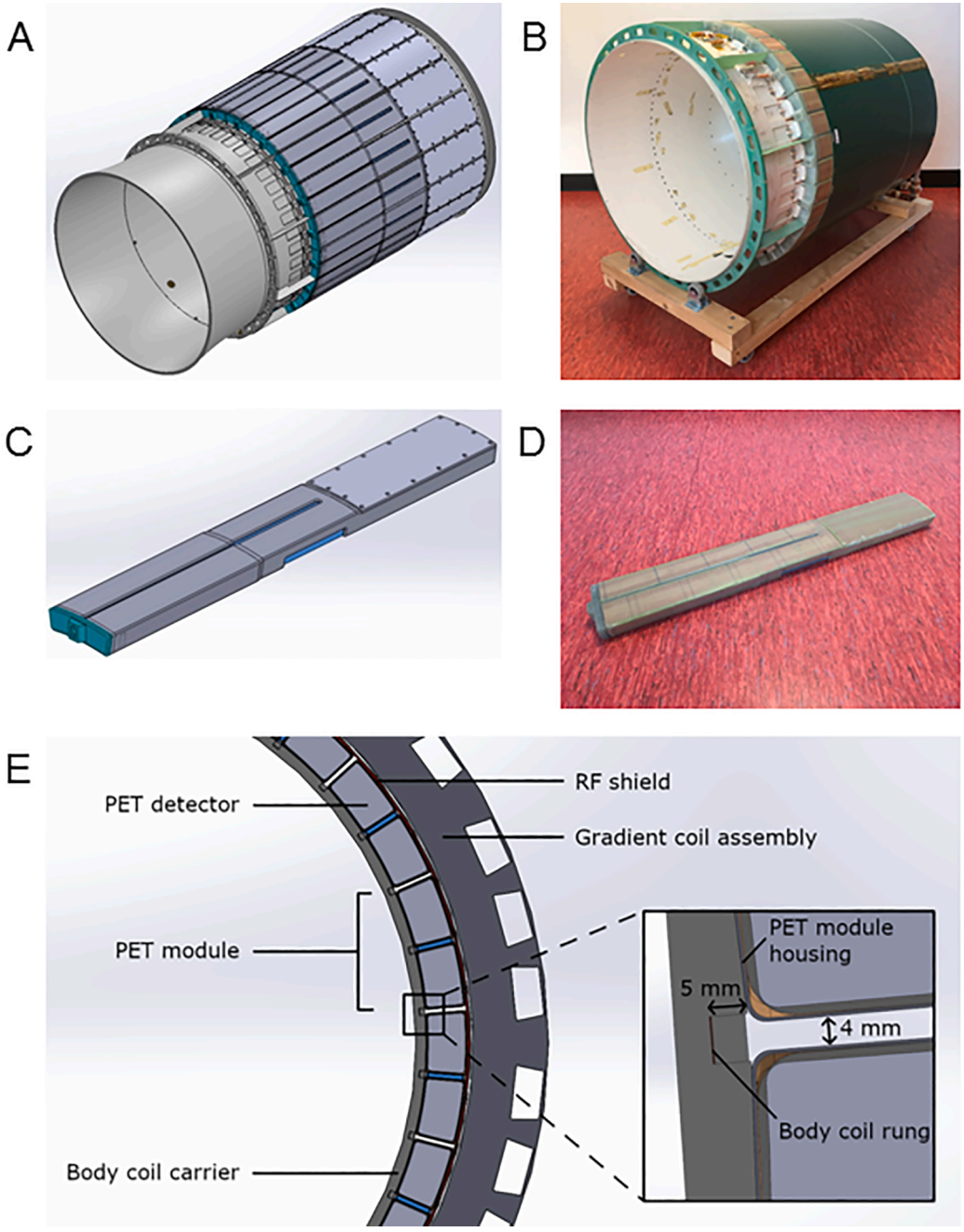

Fig. 1. Design and physical prototype of the wide-bore 1.5 T MR body coil with 19 integrated PET modules. (A) Body coil carrier with all 19 PET module housings in place. (B) Physical prototype of the body coil carrier with 19 empty PET module housings and RF shield (slightly retracted to show the housings). (C) A single PET module housing, designed to accommodate 2 separately shielded scintillation crystal rows ("fingers") and the corresponding SiPM detectors with cooling and readout electronics. (D) Physical prototype of empty PET module housing. (E) Detail drawing of the body coil design.

be divided such as to provide a perfect 90-degree drive, the deviation was very subtle maintaining low RF coupling between ports and close to circular polarization. The body coil was mounted on a body coil carrier, which was a glass fiber cylinder with an inner diameter of 65 cm and axial length 103.5 cm (Fig. 1B).

The body coil was designed to accommodate 19 integrated MRI-compatible PET detector modules constructed from the Hyperion III platform (the successor of the electronics used in the Hyperion I [17] and Hyperion II^D inserts [7]). The PET detector modules were enclosed in 0.5 mm thick glass fiber housings (Futura Composites, Heerhugowaard, the Netherlands), of which the inner surface was covered with a 0.3 mm thick layer of phosphor-bronze mesh to provide RF shielding (Fig. 1C and D). Phosphor-bronze mesh has been shown to effectively shield RF fields and block gradient-induced eddy current artifacts [18]. The phosphor-bronze mesh was tested regarding the shielding effectiveness and the distortion of the main and gradient magnetic field with the characterization methods described in [19]. Even though it was not separated by capacitors, it still provided a high gradient transparency.

To reduce the eddy currents induced in the phosphor-bronze shielding during gradient switching and RF transmission [16], the detector module housings were split up over the axial length to allow the insertion of two rows of scintillation crystals ("fingers"), such that each finger was enclosed individually in separate shielding. The gaps between two fingers were 4 mm wide and the rungs of the body coil were located behind these gaps at a radial distance of 5 mm away from the PET detector housings (Fig. 1E). The height (radial dimension) of the housings was 36 mm. The gradient RF shield, which was essentially the same as the RF shield used in the Philips Ingenia (Best, the Netherlands), fitted tightly around the PET shields, with no significant distance between the gradient RF shield and the PET detector shields (Fig. 1B).

2.2. Simulations

The effects of the PET detector housings on B_1^+ uniformity and SAR were studied by performing finite difference time domain simulations using Sim4Life (Zürich Med Tech, Zürich, Switzerland). We simulated the PET/MRI body coil with and without the presence of PET detector housings, and compared the results with simulations of the standard body coil of a clinically available wide-bore MRI system (Philips Ingenia 1.5 T). The PET detector housings were modelled as perfect electric conductors, without PET detectors or readout electronics inside. The birdcage was tuned with 38*2 capacitors (156 pF) at both end-rungs. The electronic losses in the transmit chain were simulated by adding resistors parallel to the capacitors, with resistance values chosen such as to match the B_1^+ efficiency of the simulated clinical body coil to the measurement. The simulations of the other body coils were done using the same resistance values.

For assessing the B_1^+ uniformity, the body coil was loaded with a

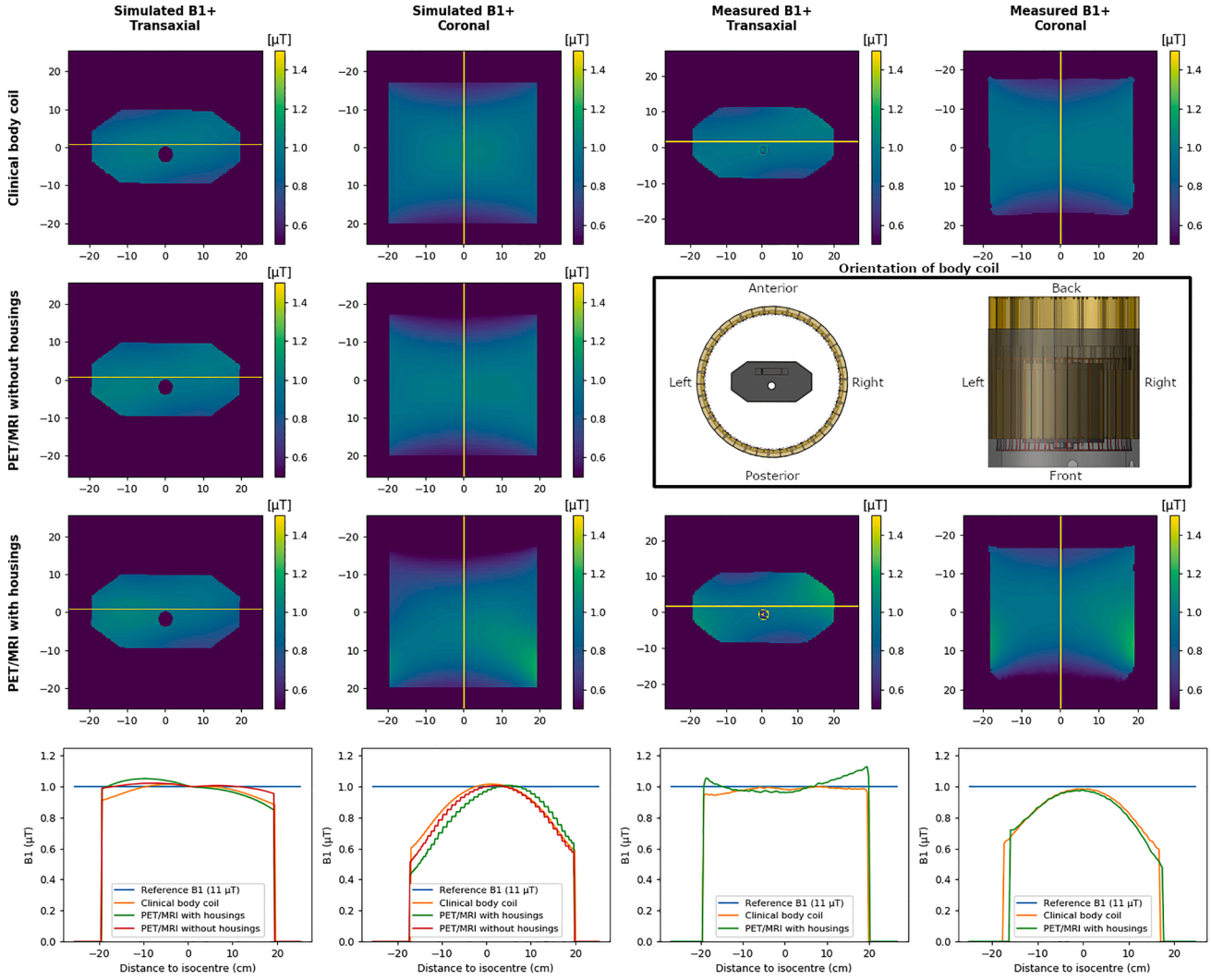

Fig. 2. Simulated and measured B_1^+ transmit field maps (central transaxial and coronal slices) and image profiles. The yellow lines in the B_1^+ maps indicate the locations of the image profiles.

Table 1
B_1^+ uniformity in the pelvis phantom.

	Simulations			Measurements		
	Transaxial slice	Coronal slice	Central volume	Transaxial slice	Coronal slice	Central volume
Clinical body coil	83.3%	72.2%	89.2%	82.6%	73.9%	80.1%
PET/MRI without PET housings	86.2%	66.3%	90.5%	not determined	not determined	not determined
PET/MRI with PET housings	80.5%	51.6%	85.6%	74.1%	46.3%	79.6%

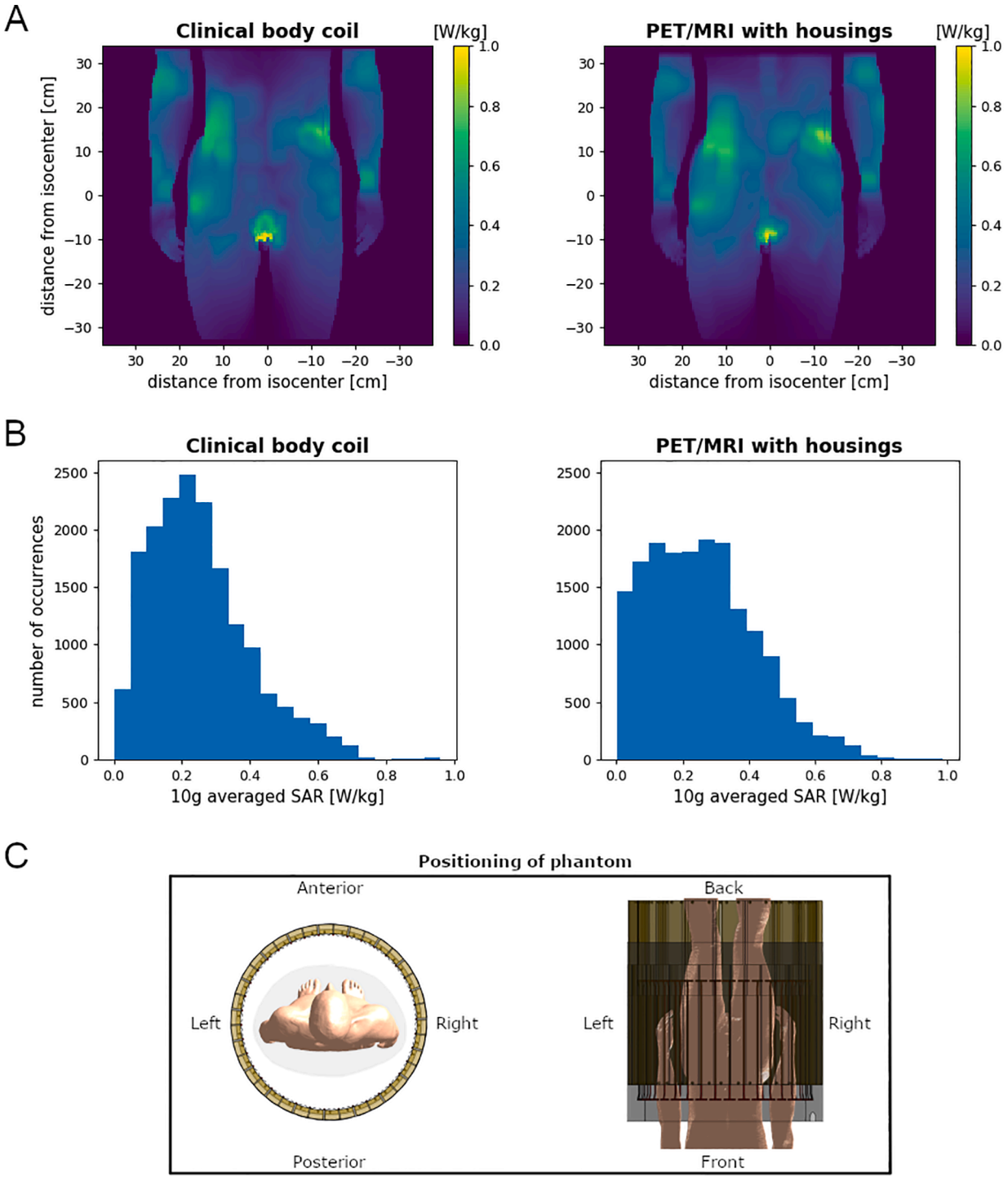

Fig. 3. Results of SAR simulations. (A) Maximum intensity plots of 10 g averaged SAR. (B) Histograms of SAR values in all non-zero voxels. (C) Positioning of phantom in PET/MRI body coil during SAR simulations.

pelvis-mimicking phantom consisting of a plastic case with outer dimensions 41 × 21 × 41 cm^3 and an inner compartment filled with polyvinylpyrrolidone (PVP) [20] (Supplemental Fig. 1A and B). B_1^+ maps were generated and normalized to achieve a reference B_1^+ field strength of 1 μT in the isocenter.

To evaluate the impact on SAR, the body coil was loaded with the human voxel model "Duke" from the Virtual Family (IT'IS Foundation, Zurich, Switzerland) [21]. According to IEC guidelines [22], 10 g averaged SAR (SAR_{10g}) maximum intensity projection images were calculated for the PET/MRI body coil with PET housings and for the clinical body coil. B_1^+ maps were again normalized to achieve a B_1^+ field strength of 1 μT in the isocenter.

2.3. Experiments

We built a prototype of the proposed body coil and positioned it in a wide-bore 1.5 T MRI system (Philips Ingenia 1.5 T). B_1^+ maps were obtained with the actual flip angle method [23] using the prototype PET/MRI body coil (with detector housings) and using the clinical body coil, both loaded with the pelvis-mimicking phantom (Supplemental Fig. 1C) and with a healthy volunteer. The study was approved by the internal review board and written informed consent was obtained from the volunteer. During the experiments, 2 prototype PET modules were present inside 2 of the 19 housings. For this study on body coil RF performance, the effect of these PET modules was assumed to be negligible. We recorded the RF input power, which was automatically adjusted by the MRI system to achieve a specified reference B_1^+ field strength in the isocenter of the scanner (11 μT for all scans). The B_1^+ efficiency was expressed as B_1^+ in the isocenter per square root of input power. For easy comparison with the simulations, the experimental B_1^+ maps of the pelvis phantom were normalized to achieve a reference B_1^+ field strength of 1 μT in the isocenter.

2.4. Data analysis

For both the simulated and experimental B_1^+ maps of the pelvis phantom, central transaxial and coronal slices were compared visually. For the experimental data, voxels outside the phantom were set to zero based on a mask obtained by thresholding the magnitude image. B_1^+ uniformity was quantified by defining regions of interest (ROIs) and calculating the following formula:

$$\text{Uniformity}(\%) = \left(1 - \frac{S_{max} - S_{min}}{S_{max} + S_{min}}\right) \times 100$$

where S_{max} and S_{min} are respectively the maximum and minimum B_1^+ value of all voxels in the ROI. Three ROIs were defined per scan:

1) Central transaxial slice: all non-zero voxels in the transaxial slices shown in Fig. 2
2) Central coronal slice: all non-zero voxels in the coronal slices shown in Fig. 2
3) Central volume: all voxel values within a 12 × 12 × 12 cm^3 cubic ROI centered on the isocenter of the scanner, excluding voxels corresponding to the air channel (we excluded all voxels in a cylinder with radius 3 cm centered on the air channel having radius 2 cm).

3. Results

3.1. B_1^+ uniformity in pelvis phantom

The experimentally measured B_1^+ transmit field maps in the phantom agreed well with the simulations (Fig. 2), which was confirmed by the quantitative data in Table 1. The coronal cross-sections showed that the PET/MRI body coil (with housings) resulted in a more asymmetric B_1^+ profile along the longitudinal axis, and to areas of increased intensity in the corners, close to the body coil, at the end where the RF birdcage

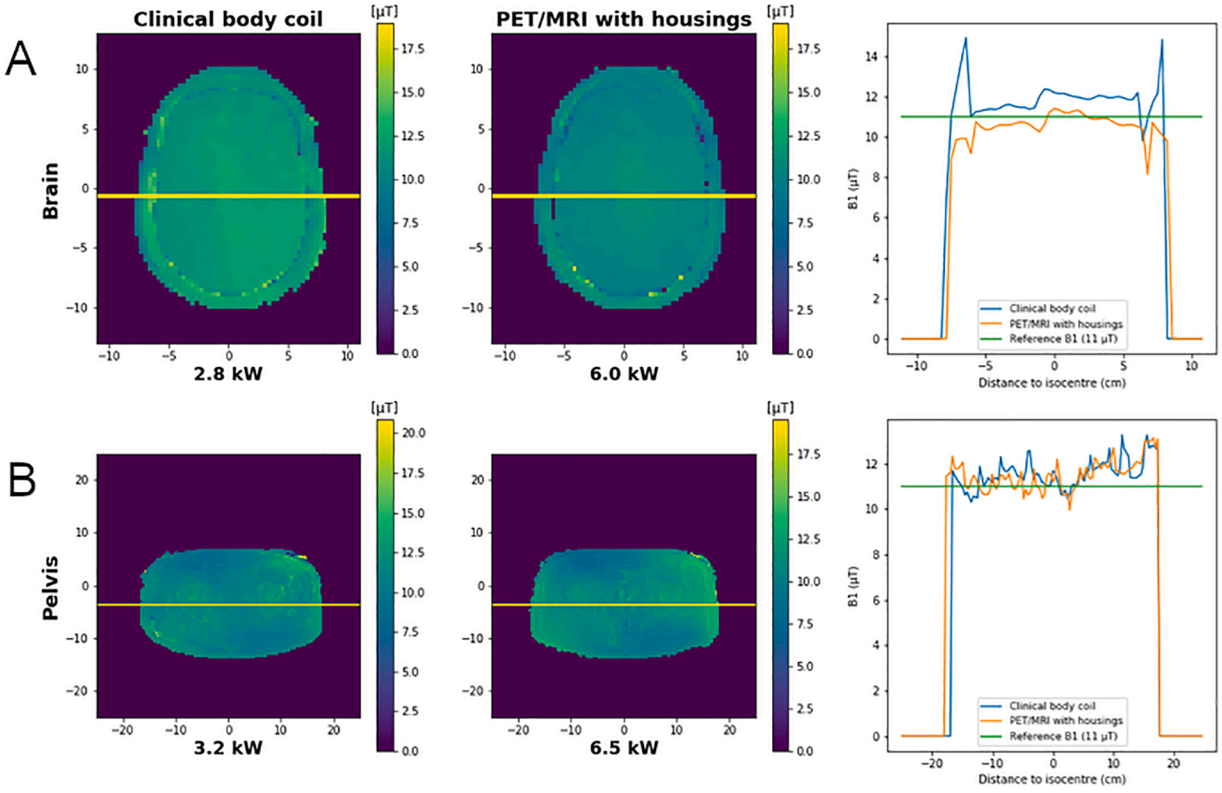

Fig. 4. B_1^+ maps and image profiles of volunteer scans. (A) Central transaxial slices through the volunteer's brain. (B) Central transaxial slices through the volunteer's pelvis. Yellow lines indicate the locations of the image profiles.

Table 2
B_1^+ efficiency in the isocenter.

Body coil	Pelvis phantom	Volunteer pelvis	Volunteer brain
Clinical body coil	0.227	0.195	0.209
PET/MRI with PET housings	0.140	0.137	0.142

Values expressed in $\mu T/\sqrt{W}$.

rungs extend beyond the PET detectors (shown left in Fig. 1A and B). The simulations of the PET/MRI body coil without PET housings showed that these differences were mostly due to the addition of the PET housings, as the effects of changing only the body coil design (more rungs and a slightly smaller diameter) were much smaller.

3.2. SAR maps in human body model

The maximum-intensity plots (MIPs) and histograms of the SAR maps simulated in the Duke phantom demonstrated that the SAR distributions were similar for both the clinical and the PET/MRI body coil with housings, with the hot spots located approximately at the same positions in the body (Fig. 3). The SAR histograms indicated that there were differences in local SAR, mostly in regions where SAR values were low. The maximum achieved local SAR values were almost equal for both body coils: 0.96 W/kg for the clinical body coil vs 0.99 W/kg for the PET/MRI body coil with detector housings. The mean voxel value was 0.14 W/kg for both body coils.

3.3. B_1^+ uniformity in volunteer

The B_1^+ maps acquired in vivo in the brain and the pelvis showed that in both the brain and the pelvis, the distributions obtained with the prototype PET/MRI body coil were almost the same as those obtained with the clinical body coil (Fig. 4). This was also confirmed by the image profiles, which were similar in shape. To achieve the same reference B_1, the PET/MRI body coil required approximately twice the power as the standard (Ingenia) body coil in both the brain and the pelvis.

3.4. B_1^+ efficiency

For respectively the pelvis phantom, the volunteer pelvis and the volunteer brain, the experimentally determined B_1^+ efficiency was 38%, 30%, and 32% less efficient for the prototype PET/MRI body coil than for the clinical body coil (Table 2). The variation in measured B_1^+ efficiencies between different loadings was larger for the clinical body coil.

4. Discussion

In this study, we introduced a new strategy to increase the inner bore diameter of whole-body simultaneous PET/MRI systems: positioning the PET detectors in the gap between the body coil conductors and the RF shield. Simulations of a prototype body coil based on this strategy showed that it can achieve nearly the same B_1^+ field uniformity as the body coil of a clinical wide-bore MRI system (Fig. 2) and a similar SAR distribution with the peak value well within the safe range (Fig. 3). The observed differences in uniformity were relatively small, located mostly at the periphery of the FOV and mainly resulting from the addition of the PET detector housings. The uniformity findings were confirmed by phantom and human volunteer measurements (Fig. 4). The B_1^+ efficiency was 38% lower compared to the clinical body coil.

Compared to the inner bore diameter of the standard wide-bore Ingenia body coil, our body coil design compromised only 3 cm, whereas currently available simultaneous whole-body PET/MRI systems compromised at least 10 cm compared to the MRI systems on which they were based [13,14]. One of these existing designs used a similar but different approach to reduce the amount of empty space between the RF conductors and the RF shield, by introducing an inward dip into the RF shield [14]. The distance between the birdcage and the RF shield was 1 cm in this system, but its inner bore diameter was still 5 cm smaller compared to our design. The bore diameter is the result of an optimization of several factors, including the thickness of the PET detector crystals and readout electronics. For our design, we assumed that the combination of crystal plus readout electronics was 35 mm thick. Comparing the impact on bore diameter between systems was not possible for each factor separately, since not all details were available in the literature (e.g. the space occupied by the readout electronics was not stated by Delso et al and Levin et al. [13,14]). Nevertheless, this study may be useful for future designs, as it demonstrated that the space between the birdcage and the RF shield could be utilized to achieve a better trade-off between bore size and PET detector thickness.

Whereas Levin et al. [14] reported a 24% increase in B_1^+ efficiency of its body coil compared to the MRI body coil without PET detectors, our body coil was 38% less efficient. The expected reduction in efficiency was most likely overcompensated by a larger efficiency increase due to the 10 cm reduction in bore diameter, which in our design was only 5 cm. The lower efficiency of our PET/MRI body coil could have an effect on the maximum B_1^+ that could be obtained given a specific RF amplifier and sample inside the body coil. In cases where the B_1^+ cannot be obtained, the RF pulses could be lengthened to obtain the desired flip angle, yet this could affect the minimum echo time that can be achieved. An alternative would be to add an additional RF amplifier and combine the RF power to the body coil, which is a standard procedure in 3 T MRI systems. The results of the SAR simulation (Fig. 3) suggested that RF power could be safely increased, as the peak SAR values for the PET/MRI body coil and the Ingenia were almost identical for an equal B_1^+ in the isocenter. The main hurdle for increasing the RF input power seemed to be the cost of additional RF amplifiers.

Our B_1^+ homogeneity maps had a similar appearance as those reported by Delso et al. [13], with flip angle values also increasing towards the birdcage rungs. In our design, the PET detector shields did not cover the entire length of the birdcage rungs (Fig. 1A and B). The effect of this was reflected in the more hyperintense areas in the front corners of the coronal slice, close to the body coil (Fig. 2). Especially these hyperintense areas caused a B_1^+ uniformity reduction of the central coronal slice by 29% in the simulations and by 37% in the measured data, compared to the clinical body coil (Table 1). This reflected only a local effect at the periphery of the FOV; in the central volume, the B_1^+ uniformity was reduced by only 4% in the simulations and 0.6% in the measurements (Table 1).

The 3-D distribution of SAR in the Duke phantom was essentially the same between the two body coil designs (Fig. 3). The small local differences between the SAR maps were most likely an effect of the addition of the housings, since the B_1^+ transmit field maps were not significantly different between the clinical body coil and the PET/MRI body coil without housings (Fig. 2). Simulations with different human models at different locations inside the body coil would provide more insight on RF safety. However, the aim of the current SAR simulations was to test whether the extra power required in the PET/MRI body coil would lead to SAR increases in the patient, and studying differences in RF safety between the coils was beyond the scope of this work.

This study focused on the effects of the PET shielding on the RF performance of our body coil design. To conclude about the feasibility of building a simultaneous PET/MRI system based on this design, a comprehensive study would be required on MRI gradient field and PET/MRI imaging performance, with all PET detectors present in the detector housings, including cabling and cooling system components, as in e.g. [7,12–14]. Experiments with physical PET detector prototypes could also demonstrate whether the shielding would be thick enough to protect the PET components from interference by strong RF pulses and gradient switching [16], or whether other methods should be included to reduce the RF interference [24].

In PET/MRI-guided radiotherapy planning, severe localization errors could result from differences in patient positioning between planning and therapy [1,2]. If certain requirements on patient positioning during radiotherapy (e.g. arms up, the use of large immobilization and positioning aids, or special RF coils or coil holders [3,4]) would not be achievable during PET/MRI due to space restrictions, larger radiation margins would be necessary to compensate for this, or the patient could not be eligible for PET/MRI-guided therapy planning at all. Moreover, experience and studies with 60 cm bore MRI systems have shown that a considerable proportion of patients are too obese to physically fit into the scanner (e.g. one study found that 10% of the patients did not fit [25]), and that the proportion of patients that cannot be imaged or require sedation due to claustrophobia was also substantial [26]. Increasing the inner bore diameter, even in the order of a couple of centimeters, would be highly beneficial because it would increase the percentage of obese and claustrophobic patients that could be imaged on the system, while reducing discomfort for all patients.

Our conclusion from this study was that the inner bore diameter of PET/MRI systems could be increased by positioning shielded PET detectors between the body coil and the RF shield, while maintaining B_1^+ field uniformity with a negligible increase of SAR. The 38% B_1^+ efficiency reduction compared to the clinical body coil could be compensated by adding a second RF amplifier to achieve the desired flip angle. This could be an important step towards achieving simultaneous PET/MRI with a relatively wide bore, which is a big advantage for application in radiotherapy planning.

Declaration of Competing Interest

The authors declare that they have no known competing financial interests or personal relationships that could have appeared to influence the work reported in this paper.

Acknowledgments

The authors would like to thank Marc Verheyen, Randy Duensing, Jurgen Mollink, and Peter van der Meulen for their advice and support during the design, development and testing of the prototype body coil. This collaboration project was co-funded by the PPP Allowance made available by Health ~ Holland, Top Sector Life Sciences & Health, to stimulate public-private partnerships.

This paper is part of a special issue that contains contributions originally submitted to the scientific meeting MR in RT, which was planned to take place 05/2020, organized by the German Research Center (DKFZ) in Heidelberg. We acknowledge funding by DKFZ for the publication costs of this special issue.

Appendix A. Supplementary data

Supplementary data to this article can be found online at https://doi.org/10.1016/j.phro.2020.12.002.

References

[1] Thorwarth D, Leibfarth S, Mönnich D. Potential role of PET/MRI in radiotherapy treatment planning. Clin Transl Imaging 2013;1:45–51. https://doi.org/10.1007/s40336-013-0006-2.
[2] Zhu T, Das S, Wong TZ. Integration of PET/MR hybrid imaging into radiation therapy treatment. Magn Reson Imaging Clin N Am 2017;25:377–430. https://doi.org/10.1016/j.mric.2017.01.001.
[3] Paulus DH, Oehmigen M, Grueneisen J, Umutlu L, Quick HH. Whole-body hybrid imaging concept for the integration of PET/MR into radiation therapy treatment planning. Phys Med Biol 2016;61:3504. https://doi.org/10.1088/0031-9155/61/9/3504.
[4] Brynolfsson P, Axelsson J, Holmberg A, Jonsson JH, Goldhaber D, Jian Y, et al. Technical note: adapting a GE SIGNA PET/MR scanner for radiotherapy. Med Phys 2018;45:3546–50. https://doi.org/10.1002/mp.13032.
[5] Winter RM, Leibfarth S, Schmidt H, Zwirner K, Mönnich D, Welz S, et al. Assessment of image quality of a radiotherapy-specific hardware solution for PET/MRI in head and neck cancer patients. Radiother Oncol 2018;128:485–91. https://doi.org/10.1016/j.radonc.2018.04.018.
[6] Delso G, Ziegler S. PET/MRI system design. Eur J Nucl Med Mol Imaging 2009;36:86–92. https://doi.org/10.1007/s00259-008-1008-6.
[7] Weissler B, Gebhardt P, Dueppenbecker PM, Wehner J, Schug D, Lerche CW, et al. A digital preclinical PET/MRI insert and initial results. IEEE Trans Med Imaging 2015;34:2258–70. https://doi.org/10.1109/TMI.2015.2427993.
[8] Wehner J, Weissler B, Dueppenbecker PM, Gebhardt P, Goldschmidt B, Schug D, et al. MR-compatibility assessment of the first preclinical PET-MRI insert equipped with digital silicon photomultipliers. Phys Med Biol 2015;60:2231–55. https://doi.org/10.1088/0031-9155/60/6/2231.
[9] Omidvari N, Topping G, Cabello J, Paul S, Schwaiger M, Ziegler SI. MR-compatibility assessment of MADPET4: a study of interferences between an SiPM-based PET insert and a 7 T MRI system. Phys Med Biol 2018;63:095002. https://doi.org/10.1088/1361-6560/aab9d1.
[10] Jung JH, Choi Y, Jung J, Kim S, Lim HK, Im KC, et al. Development of PET/MRI with insertable PET for simultaneous PET and MR imaging of human brain: development of PET/MRI with insertable PET. Med Phys 2015;42:2354–63.
[11] Kolb A, Wehrl HF, Hofmann M, Judenhofer MS, Eriksson L, Ladebeck R, et al. Technical performance evaluation of a human brain PET/MRI system. Eur Radiol 2012;22:1776–88. https://doi.org/10.1007/s00330-012-2415-4.
[12] Lee BJ, Grant AM, Chang C-M, Watkins RD, Glover GH, Levin CS. MR performance in the presence of a radio frequency-penetrable positron emission tomography (PET) insert for simultaneous PET/MRI. IEEE Trans Med Imaging 2018;37:2060–9. https://doi.org/10.1109/TMI.2018.2815620.
[13] Delso G, Furst S, Jakoby B, Ladebeck R, Ganter C, Nekolla SG, et al. Performance measurements of the Siemens mMR integrated whole-body PET/MR scanner. J Nucl Med 2011;52:1914–22. https://doi.org/10.2967/jnumed.111.092726.
[14] Levin CS, Maramraju SH, Khalighi MM, Deller TW, Delso G, Jansen F. Design features and mutual compatibility studies of the time-of-flight PET capable GE SIGNA PET/MR system. IEEE Trans Med Imaging 2016;35:1907–14. https://doi.org/10.1109/TMI.2016.2537811.
[15] Disselhorst JA, Bezrukov I, Kolb A, Parl C, Pichler BJ. Principles of PET/MR Imaging. J Nucl Med 2014;55:2S–10S. https://doi.org/10.2967/jnumed.113.129098.
[16] Vandenberghe S, Marsden PK. PET-MRI: a review of challenges and solutions in the development of integrated multimodality imaging. Phys Med Biol 2015;60:R115–54. https://doi.org/10.1088/0031-9155/60/4/R115.
[17] Weissler B, Gebhardt P, Lerche CW, Wehner J, Solf T, Goldschmidt B, et al. MR compatibility aspects of a silicon photomultiplier-based PET/RF insert with integrated digitisation. Phys Med Biol 2014;59:5119–39. https://doi.org/10.1088/0031-9155/59/17/5119.
[18] Lee BJ, Watkins RD, Chang C-M, Levin CS. Low eddy current RF shielding enclosure designs for 3T MR applications: Low Eddy Current RF Shielding. Magn Reson Med 2018;79:1745–52. https://doi.org/10.1002/mrm.26766.
[19] Gross-Weege N, Dey T, Gebhardt P, Schug D, Weissler B, Schulz V. Characterization methods for comprehensive evaluations of shielding materials used in an MRI. Med Phys 2018;45:1415–24. https://doi.org/10.1002/mp.12762.
[20] Ianniello C, de Zwart JA, Duan Qi, Deniz CM, Alon L, Lee J-S, et al. Synthesized tissue-equivalent dielectric phantoms using salt and polyvinylpyrrolidone solutions: synthesized tissue-equivalent dielectric properties using a water-soluble polymer. Magn Reson Med 2018;80:413–9. https://doi.org/10.1002/mrm.27005.
[21] Christ A, Kainz W, Hahn EG, Honegger K, Zefferer M, Neufeld E, et al. The virtual family—development of surface-based anatomical models of two adults and two children for dosimetric simulations. Phys Med Biol 2010;55:N23–38. https://doi.org/10.1088/0031-9155/55/2/N01.
[22] IEC. Medical Electrical Equipment. Part 2-33: Particular Requirements for the Safety of Magnetic Resonance Equipment for Medical Diagnosis. IEC 60601-2-33; 2010.
[23] Yarnykh VL. Actual flip-angle imaging in the pulsed steady state: a method for rapid three-dimensional mapping of the transmitted radiofrequency field. Magn Reson Med 2007;57:192–200. https://doi.org/10.1002/mrm.21120.
[24] Gebhardt P, Wehner J, Weissler B, Botnar R, Marsden PK, Schulz V. FPGA-based RF interference reduction techniques for simultaneous PET–MRI. Phys Med Biol 2016;61:3500–26. https://doi.org/10.1088/0031-9155/61/9/3500.
[25] Corwin A, Aresty A, Chong S, Brunsvold M, Evans JR, Gillespie RB, et al. Will they fit? Development of a measurement device to assess body habitus compatibility with MRI bore diameter for emergency trauma imaging. Emerg Radiol 2012;19:141–8. https://doi.org/10.1007/s10140-011-1010-3.
[26] Dewey M, Schink T, Dewey CF. Claustrophobia during magnetic resonance imaging: cohort study in over 55,000 patients. J Magn Reson Imaging 2007;26:1322–7. https://doi.org/10.1002/jmri.21147.